PHYSICS

Multi-stimulus perception and visualization by an intelligent liquid metal-elastomer architecture

Hongzhang Wang[1,2]*†, Bo Yuan[2,3]†, Xiyu Zhu[2], Xiaohui Shan[2], Sen Chen[4], Wenbo Ding[5], Yingjie Cao[2], Kaichen Dong[1,5], Xudong Zhang[6], Rui Guo[2], Yuchen Yao[6], Bo Wang[2,3], Jianbo Tang[7]*, Jing Liu[2,6]*

Multi-stimulus responsive soft materials with integrated functionalities are elementary blocks for building soft intelligent systems, but their rational design remains challenging. Here, we demonstrate an intelligent soft architecture sensitized by magnetized liquid metal droplets that are dispersed in a highly stretchable elastomer network. The supercooled liquid metal droplets serve as microscopic latent heat reservoirs, and their controllable solidification releases localized thermal energy/information flows for enabling programmable visualization and display. This allows the perception of a variety of information-encoded contact (mechanical pressing, stretching, and torsion) and noncontact (magnetic field) stimuli as well as the visualization of dynamic phase transition and stress evolution processes, via thermal and/or thermochromic imaging. The liquid metal-elastomer architecture offers a generic platform for designing soft intelligent sensing, display, and information encryption systems.

INTRODUCTION

Soft materials with multi-stimulus responsiveness and integrated functionalities have been increasingly used in advanced robotics (*1*, *2*), flexible electronics (*3*, *4*), soft sensors (*5*), actuators (*6*, *7*), information display (*8*–*10*), and biomedical adhesives (*11*, *12*), in pursuit of biological compliance and biomimetic functions (*13*, *14*) and, ultimately, soft intelligence (*15*, *16*). Soft materials with embedded intelligence are expected to be able to perceive the surrounding environment and react to external changes and applied stimuli in controllable and programable ways (*2*, *17*, *18*). Incorporating microscopic inclusions (fillers) into a soft matrix is a powerful yet versatile strategy for introducing properties extrinsic to the host material, thus achieving non-inherited functionalities (*19*, *20*). Despite previous successful demonstrations of a variety of soft systems with intriguing properties (*21*, *22*), such a composite engineering approach is strongly restricted when intelligent behaviors and their integration are targeted in design (*23*). This is primarily because individual fillers usually play a single defined role in modifying material properties, while using more than one filler will result in systematic complexity and even incompatibility that compromise the whole design. Therefore, it is challenging but highly desirable to devise a soft architecture with integrated intelligent functionalities and structural simplicity, which is the first step toward the overarching goal of soft intelligence.

Liquid metals, in the form of micro/nanodroplets, have emerged as unique filler materials owing to their unrivaled coupled fluidic and metallic properties (*24*–*28*). Liquid metal-embedded soft materials with high electrical and thermal conductivity (*29*, *30*), tunable conductivity (*31*–*33*), and self-healing capability (*34*) have been reported. In most cases, the tuning of thermal, electrical, or mechanical properties of the soft materials by highly conductive yet conformable liquid metal inclusions is focused (*34*–*37*). Liquid metals' high volumetric latent heat, which can be used as a regenerative energy source, has been largely overlooked to date. For example, room temperature liquid metal gallium (Ga) has an exceedingly high volumetric latent heat of 473 kJ/liter (for comparison, that of water is 336 kJ/liter). In previous reports where the phase transition of liquid metal is concerned, efforts are mainly devoted to mechanistic investigation and thermal analysis (*38*–*41*). In addition, the strong supercooling tendency of liquid Ga and the stimuli-sensitive nature of its solidification further provide the opportunity for on-demand control of its phase transition (*42*–*44*) and latent heat release. However, it is previously believed that the solidification of dispersed liquid metal droplets in a soft matrix should result in a temperature change that is largely unnoticeable (*38*), and the strong supercooling of the liquid metal inclusion can be challenging to overcome (*43*, *45*). We hypothesize that, when released into a soft material matrix with a much lower thermal conductivity than that of the liquid metal inclusion, the latent heat generated during the solidification of liquid metal can be leveraged for thermal imaging, which provides a mechanism for multi-stimulus perception and visualization. Directly yet remotely visualizing and imaging thermal energy flow as the information carrier can be advantageous in comparison to the current dominant strategies based on electrical feedback signals.

Here, we demonstrated that the liquid-to-solid phase transition of liquid metals enabled perception and response mechanisms of a liquid metal-elastomer architecture (LMEA) when subject to various forms of mechanical (contact) and magnetic (noncontact) stimuli. The controllable solidification of the magnetized liquid metal droplet inclusion led to localized transient latent heat release and established thermal gradients within the elastomer matrix. This

[1]Institute of Materials Research, Center of Double Helix, Shenzhen International Graduate School, Tsinghua University, Shenzhen 518055, P. R. China. [2]Department of Biomedical Engineering, Tsinghua University, Beijing 100084, P. R. China. [3]School of Mechanical Engineering and Automation, Beihang University, Beijing 100191, P. R. China. [4]Key Laboratory for Intelligent Nano Materials and Devices of Ministry of Education, and Institute for Frontier Science, Nanjing University of Aeronautics and Astronautics, Nanjing 210016, P. R. China. [5]Tsinghua-Berkeley Shenzhen Institute, Institute of Data and Information, Shenzhen International Graduate School, Tsinghua University, Shenzhen, Guangdong 518055, P. R. China. [6]Key Laboratory of Cryogenic Science and Technology, Technical Institute of Physics and Chemistry, Chinese Academy of Sciences, Beijing 100190, P. R. China. [7]School of Chemical Engineering, University of New South Wales (UNSW), Kensington, NSW 2052, Australia.
*Corresponding author. Email: wanghz@sz.tsinghua.edu.cn (H.W.); jianbo.tang@unsw.edu.au (J.T.); jliubme@tsinghua.edu.cn (J.L.)
†These authors contributed equally to this work.

allowed us to engineer a highly stretchable soft composite architecture with the capabilities of perceiving and visualizing various types of information-encoded stimuli. The concept was first demonstrated with Ga liquid metal inclusion and then extended to other binary and ternary low melting temperature alloys. We realized both thermal [infrared (IR)] and thermochromic imaging of a variety of programable liquid metal phase transition behaviors and patterns. We further demonstrated unprecedented self-recognition and display of stress distribution and evolution by the soft architecture under applied stimuli. In addition, Joule heating and IR heating, which are complementary to stimulus-induced solidification, were introduced to melt the solidified liquid metal inclusion and realize two-way control of liquid metal phase transition.

RESULTS

The LMEA consists of methyl vinyl polysiloxane/Pt-catalyzed polymethylhydrosiloxane and magnetized liquid metal droplets as the soft elastomer matrix and the phase change inclusion (Fig. 1A), respectively. Ga (melting point $T_m = 29.8°C$) was first selected to ensure that the phase transition (melting/solidification) of liquid metal could be readily realized at around room temperatures. To make

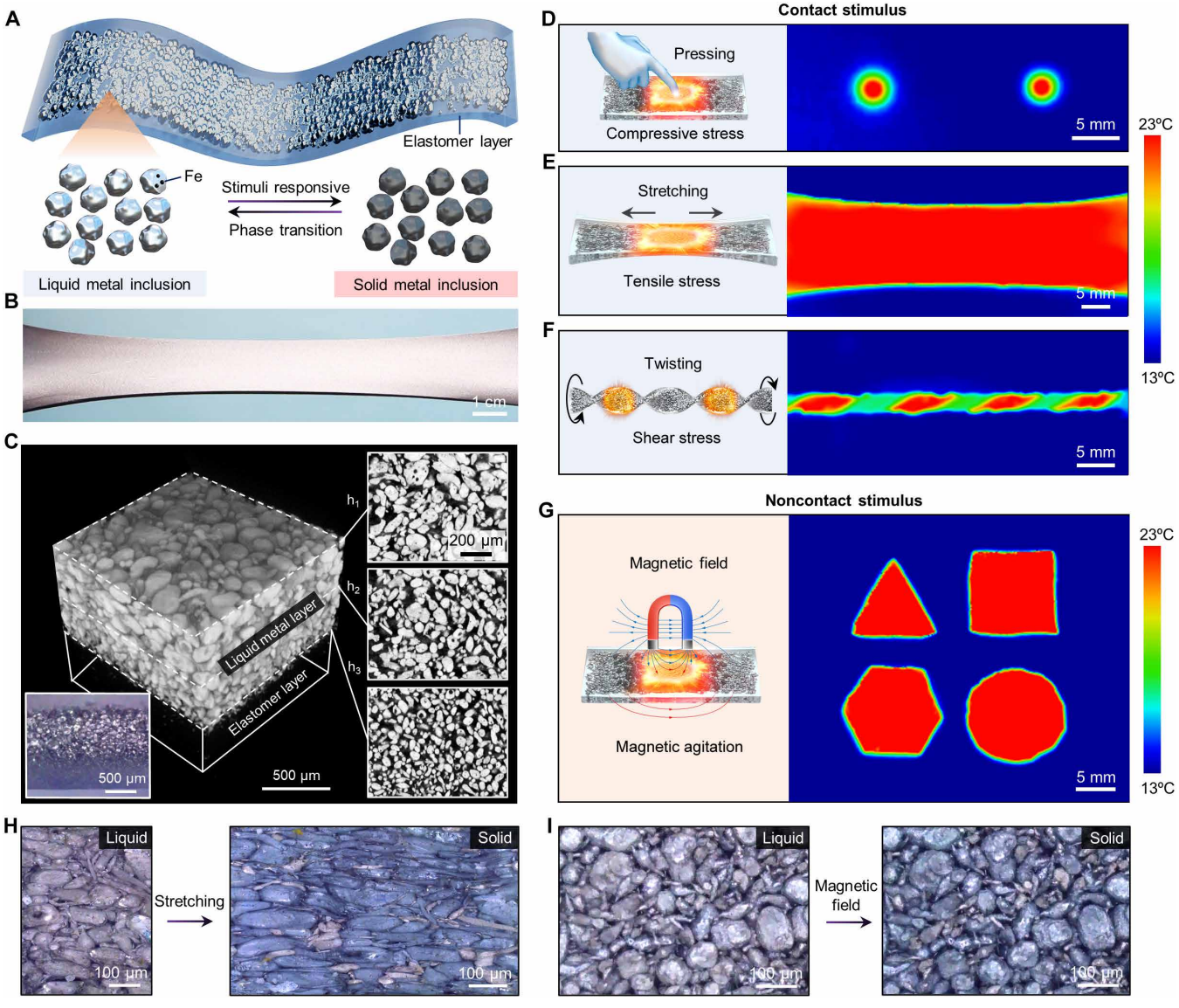

Fig. 1. Structure of the LMEA and its multi-stimulus–induced phase transition and heat release. (**A**) Schematics of LMEA with Fe-incorporated liquid metal droplets as the phase transition inclusion. (**B**) Highly stretchable LMEA under 400% strain. (**C**) Micro–computed tomography (micro-CT) image displaying the three-dimensional microstructure of LMEA. The sectional scans on the right of its upper surface, middle plane, and bottom surface show the size distributions of liquid metal droplets along the direction perpendicular to the surface planes. The bottom-left inset is a cross-sectional optical image of the sample. During sample preparation, the samples in both images were in an upside-down position. (**D** to **G**) Schematic images (left) and IR images (right) showing the solidification-induced temperature increases of the LMEA triggered by mechanical pressing (D), stretching (200% strain) (E), twisting (F), and a 200-mT magnetic field (G). The solidification of supercooled Fe-containing Ga droplets in the elastomer when mechanically stretched (elongated) by 120% strain (**H**) and applying a magnetic field (**I**).

the intrinsically paramagnetic Ga magnetically susceptible, ferromagnetic iron (Fe) particles were incorporated into the liquid Ga droplets via an intermetallic wetting mechanism (*46*). The mixing ratio of each component is detailed in Materials and Methods. Such a LMEA was highly stretchable due to both the excellent stretchability of the elastomer and the liquid-like conformability of the Ga droplet inclusion (Fig. 1B). The liquid metal droplets supercooled and behaved as microscopic latent heat reservoirs in the LMEA. When triggered externally, the solidification of these numerous liquid metal droplets released their latent heat into their hosting elastomer matrix. Because of the low thermal conductivity of the elastomer (0.29 Wm^{-1} K^{-1}), the heat was "trapped" within the material, which is favorable for maintaining a long thermal imaging/display period. During these processes, the phase transition latent heat stored in the microscopic liquid metal reservoirs was released as detectable information in the form of thermal energy flow, which was used for multi-stimulus perception and visualization purposes. The in-plane size distribution of the liquid metal droplets was relatively uniform in the LMEA but that in the direction perpendicular to the surface planes varied considerably (Fig. 1C and fig. S1), as a result of size-dependent sedimentation (Stokes law) of the liquid metal droplets during the curing of the elastomer (*31*). This also generated an elastomer-rich layer on one side of the sample (Fig. 1C). The side accumulated with liquid metal droplets was able to generate a larger amount of latent heat, which was used for phase transition investigation and thermal imaging in this study unless otherwise specified.

The LMEA showed fast response to a wide range of solidification triggers, and the accompanying transient latent heat release was revealed by thermal imaging (Fig. 1, D to G). Different forms of mechanical agitations (*47*) including pressing (Fig. 1D), stretching (Fig. 1E), and twisting (Fig. 1F) were used as contact stimuli to initiate the solidification of the liquid metal inclusion. The control experiment using only the elastomer (without the liquid metal inclusion) showed negligible temperature change (fig. S2), ruling out the contribution of the elastomer's elastocaloric effect to the observed temperature increase. Localized temperature increase at an arbitrary location of the sample could be generated by pressing at selected locations (Fig. 1D). It was also feasible to solidify individual droplets (fig. S3), suggesting that the highest phase transition resolution of the material could be comparable to the characteristic size of the Ga droplets (~100 μm). The actual resolution of thermal imaging was slightly lower due to inevitable thermal diffusion (fig. S4). When the material was under stretching or twisting, the embedded liquid metal droplets collectively experienced a tensile or a torsion stress, which resulted in a global phase transition and a uniform temperature increase across the specimen (Fig. 1, E and F, and movie S1). The twisted elastomer intermittently displayed its two sides which featured distinct droplet packing density. Consequently, successive high and low temperature segments corresponding to the densely packed liquid metal side and the elastomer-rich side of the LMEA, respectively, were observed in Fig. 1F. Apart from contact mechanical stimuli, a noncontact magnetic field (generated by a permanent magnet) also readily initiated the solidification and heat release of the Fe-incorporated liquid metal droplets (Fig. 1G). By shaping the liquid metal inclusion into different geometries, predefined thermal patterns were generated, which remained visible and distinguishable for over 120 s (fig. S5 and movie S2). In the LMEA, the discrete liquid metal droplets are separated by a Ga oxide layer and an elastomer layer (fig. S6). These two physical barriers prevent the merging of the droplets under both mechanical and magnetic agitations after multiple melting-solidification cycles (figs. S7 and S8). Therefore, the thermal patterns of the same sample were reproducible after repeated usage (fig. S9). The multi-stimulus responsiveness of the LMEA offers an unprecedented degree of freedom for controllable yet programable thermal display and IR patterning. The temperature of the LMEA increased to its maximum typically in seconds under both contact and noncontact stimuli. The generated heat eventually dissipated into the ambient environment, but the heat dissipation and temperature decrease processes were considerably slower in comparison to the heat release and temperature increase. Because of the asymmetric distribution of the liquid metal droplets within the LMEA, the temperature evolution of the surface on the elastomer-rich layer side showed a delay to that of the liquid metal layer, in both our finite element modeling and experimental measurement (note S1, table S1, and fig. S10) (*48*).

The incorporation of Fe particles into the Ga droplets was crucial for achieving multi-stimulus response as the particles facilitated the solidification of Ga under not only a magnetic field but also mechanical stimuli. The magnetization curve (fig. S11) and the x-ray diffraction patterns (fig. S12) of LMEA confirmed the presence of Fe, and the energy dispersive spectrometer (EDS) images of a cross section of a liquid metal droplet revealed that the Fe particles were embedded into the droplet (fig. S13). In the absence of the Fe particles, temperature increase was not observed under the same condition (stretching; fig. S14), which explains previous observations (*43*, *45*). A fraction of droplets in our system, typically the small ones, were not observed to solidify (Fig. 1, H and I), likely due to the absence of Fe particles in these droplets. In addition, it was equally important to internalize the Fe particles in the Ga droplets so that the agitation of the Fe particles directly resulted in the agitation of the liquid metal. Our control experiments using liquid Ga droplets with Fe particles spread outside did not solidify when the specimen was under the same and doubled magnetic field strength (fig. S15). Optical microscopy observation revealed the fast solidification process of the liquid metal droplets under stretching (Fig. 1H) and magnetic agitation (Fig. 1I, fig. S16, and movie S3). It is believed that the mechanism that underlies both mechanical stimulus-induced and magnetic field–induced nucleation of the supercooled liquid metal droplets is the introduction of energy fluctuations in the form of mechanical agitations (*47*).

Differential scanning calorimetry (DSC) measurement showed that the Fe particles dispersed in the liquid metal droplets shifted the nucleation pathways from homogeneous nucleation toward heterogeneous nucleation. Consequently, the Fe particles considerably suppressed the supercooling effect of the liquid metal droplets and increased their solidification onset temperature by 20°C, from −38°C (Fe absent) to −17°C (Fe present) (Fig. 2A). The Fe-containing Ga droplets still showed a considerable degree of supercooling, which ensured that autonomous solidification under ambient conditions would not occur. Nevertheless, homogeneous nucleation of part of the liquid metal droplets was observed, which was expected to be the solidification path taken by the droplets free of embedded Fe particles. The multiple small exothermic peaks of the DSC curves are characteristic solidification behavior of numerous discrete liquid metal droplets in the LMEA (Fig. 2A). An endothermic peak located at around −40°C was observed for both the elastomer and the LMEA, which was attributed to the glass transition of the elastomer. A small endothermic peak with an onset temperature of −16.3°C was

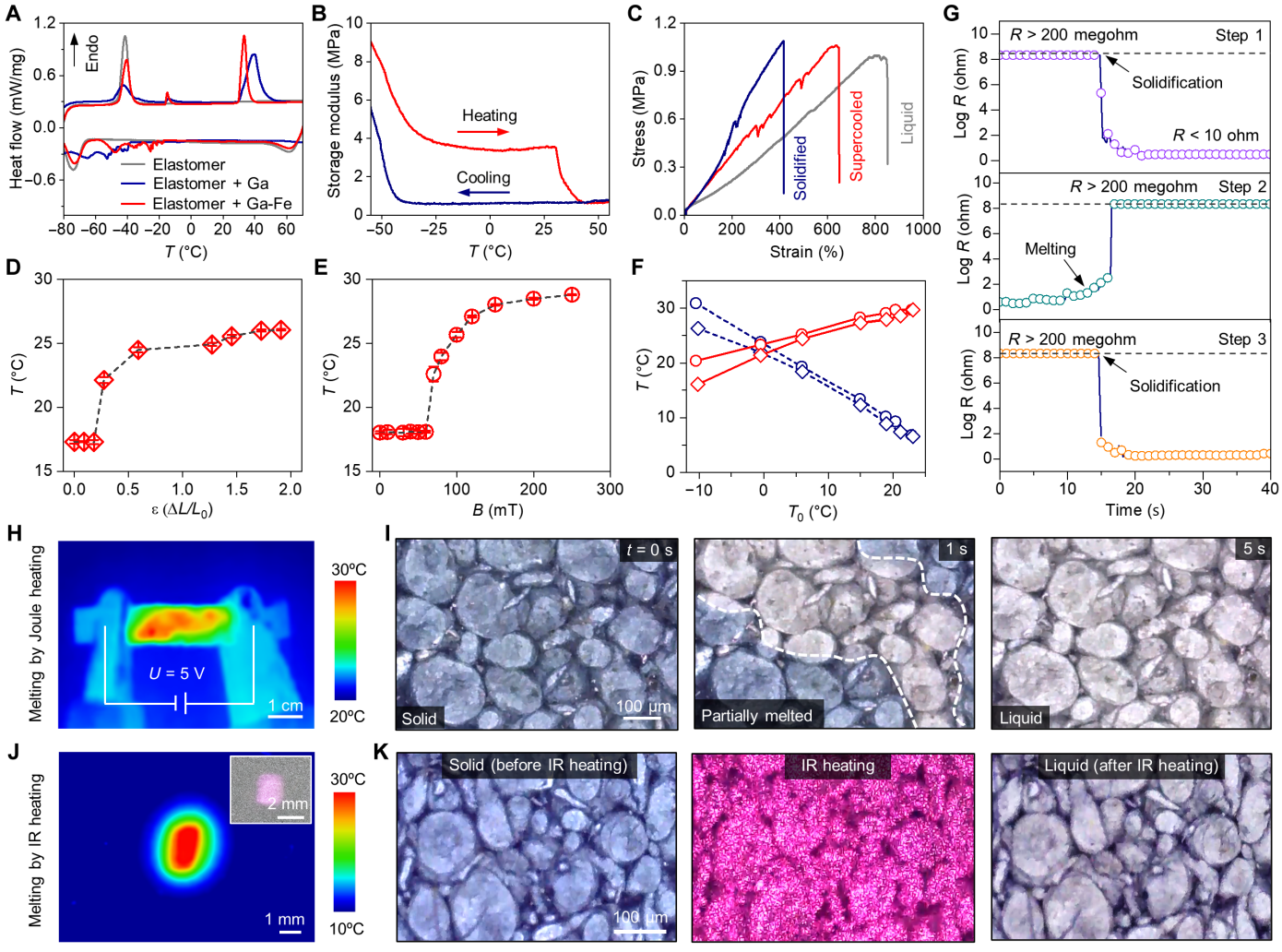

Fig. 2. Characterizations of the thermal, mechanical properties and phase transitions of the LMEA. (**A**) DSC curves of elastomer and LMEA. (**B**) The change in storage modulus of LMEA during melting and solidification. (**C**) Stress-strain curves of LMEA with liquid, supercooled, and solidified liquid metal inclusions. (**D** and **E**) The temperature change of LMEA as a function of tensile strain $\varepsilon = \Delta L/L_0$ (D) and applied magnetic field strength B (E). (**F**) Comparison of the maximum temperature T_{max} (red line) and the maximum temperature change ΔT (blue dotted line) of LMEA as a function of initial temperature T_0 triggered by mechanical (stretching) and magnetic stimuli. (**G**) Abrupt electrical resistance switching of a LMEA sample during the phase change (solidification and melting) of its liquid metal inclusion. (**H**) IR images showing the temperature increase of the LMEA under a 5-V voltage. (**I**) Time-lapse microscopy images showing the melting of the liquid metal droplets as evidenced by their color change. (**J**) IR image and optical image (inset) showing the localized temperature increase of the LMEA at the IR laser spot. (**K**) Optical microscopy images showing liquid metal droplets melting by IR laser heating.

observed for the LMEA samples regardless of the presence of Fe, which possibly originated from the interaction between the liquid metal surface oxide with the elastomer.

The mechanical properties of the LMEA were characterized by measuring the solidification-induced alterations in both its storage modulus (Fig. 2B) and elastic modulus (Fig. 2C). When the sample was cooled below −30°C, both the solidification of the Ga inclusion and the glass transition of the elastomer contributed to the storage modulus increase (Fig. 2B), and the latter was compensated (with minimal hysteresis) when the sample was heated up back to −30°C. An abrupt decrease of storage modulus from about 3.5 to 0.7 MPa was measured upon melting the solidified Ga at 30°C. The stress-strain curves displayed that the state of the liquid metal inclusion also had a considerable influence on the maximum strain of the LMEA but not its maximum tensile stress (Fig. 2C). The samples with liquid and solid Ga inclusion showed a maximum strain of >800 and 400%, which corresponded to a calculated elastic modulus of 81 and 241 kPa, respectively. A specimen with supercooled liquid Ga inclusion (testing temperature, 15°C) was further measured, which allowed liquid Ga to solidify during the tensile test. This specimen showed a maximum strain slightly over 600% which intersected that of the samples with solid and liquid Ga inclusions, and its enhanced fluctuations in the stress-strain curve were indicative of the gradual solidification of the Ga inclusion and mechanical stiffening of the material during the test. Because of the asymmetric distribution of the liquid metal droplets, asymmetric mechanical deformation (coiling) and stiffening were observed when the LMEA strips were released after being stretched to allow liquid metal solidification.

Varying the length-to-width ratio of the samples generated distinct coiling regimes (fig. S17) (*49*). Combining remote IR melting, such a reversible shape morphing mechanism was used as a shape memory effect to realize object gripping, maneuvering, and releasing (fig. S18).

The critical (threshold) strain rate (ε_c) and magnetic field strength (B_c) that required to trigger the solidification of liquid metal inclusion were measured. The temperature of the LMEA started to increase when the strain rate reached 18% or higher (Fig. 2D), indicating the start of collective solidification of liquid Ga at this threshold strain rate. The threshold magnetic field strength for triggering effective liquid metal solidification was found to be 60 mT (Fig. 2E). The relatively low threshold strain rate and magnetic field strength implied that the material was sensitive to both types of stimuli in terms of phase transition initiation and heat release. Increasing ε and B in general led to a higher temperature increase, due to the solidification of a larger amount of liquid metal droplets, until a sufficiently high strain rate (e.g., $\varepsilon > 150\%$) or magnetic field strength (e.g., $B > 200$ mT) was reached. Under high ε and B, the maximum temperature increase (T_{max}) was obtained. The LMEA showed a smaller maximum temperature increase when the solidification was triggered mechanically by stretching than by a magnetic field, suggesting that the latter was more effective in initiating liquid metal solidification.

The temperature (T_0) at which measurable solidification took place defined the applicable temperature range of the LMEA. When Ga was used as the liquid metal phase-change inclusion, a T_0 ranging from −10° to 23°C was accessed to investigate the influence of T_0 on the highest temperature T_{max} and the corresponding maximum temperature increment (ΔT_{max}) of the material. It became challenging to solidify the liquid Ga droplets above 23°C (low supercooling) either by mechanical stretching or magnetic agitation. While higher T_0 generally resulted in higher T_{max}, the maximum temperature increment ΔT_{max} was reduced when T_0 was increased (Fig. 2F). Higher T_{max} and ΔT were observed again when the solidification was induced by magnetic agitation than by mechanical stretching.

To extend the applicable temperature ranges, we further selected other liquid metals with different phase transition temperatures. Binary eutectic gallium-indium (EGaIn; $T_m = 15.4$°C), ternary eutectic gallium-indium-tin (Galinstan; $T_m = 10.6$°C), and eutectic bismuth-indium-tin (Field's metal; $T_m = 62$°C) were used to replace Ga for fabricating different Fe-incorporated LMEAs, which showed multi-stimulus responses similar to the Ga-elastomer case (fig. S19). Owing to their different melting and solidification characteristics, introducing these liquid metal alloys allowed us to use the LMEAs at different temperature ranges. For instance, $T_0 = 4$°C and $T_{max} = 11$°C were achieved with the EGaIn-elastomer architecture (fig. S19A). That for the Galinstan-elastomer architecture and the Field's metal-elastomer architecture were further extended to $T_0 = -30$°C and $T_{max} = 4$°C (fig. S19B) and $T_0 = 25$°C to $T_{max} = 50$°C (fig. S19C), respectively. Different elastomers including polydimethylsiloxane (PDMS) and Ecoflex (fig. S20) were also used as the host matrix to demonstrate that our concept can be generally extended to other soft material systems.

Apart from latent heat release, change in electrical properties can accompany the liquid metal phase transition. We found that the solidification of the liquid metal inclusion was able to reduce the resistance of the material by eight orders of magnitude, from over 200 megohm to below 10 ohm (Fig. 2G and fig. S21). Such a marked resistance change was caused by the volumetric expansion of the Ga droplets during their liquid-to-solid phase transition, which established conductive paths within the droplet network. The sample reattained its high-resistance state after remelting its liquid metal inclusion. On the basis of such a magnetic field–induced switchable transition between distinctive conducting states, a remotely (noncontact) controllable switch without any macroscopic moving component was demonstrated (fig. S22).

By virtue of physical phase transition, the materials can be reused once the solidified liquid metal inclusion was remelted and supercooled, without compromising its performance after 100 cycles (fig. S23). The same sample was also able to function normally after being stored under ambient conditions for more than 1 year, showing excellent stability of the material system (fig. S23). We introduced two strategies, namely, Joule (electrical) heating and IR heating, to melt the solidified liquid metal droplets in the LMEA. Complementary to stimulus-induced solidification, this melting step allowed us to realize bidirectional control of the liquid-to-solid phase transition, which greatly expands the applicability of the LMEA. Applying a several-volt voltage (e.g., 5 V) generated Joule heat sufficient to melt the solidified liquid metal droplets (Fig. 2H and fig. S24), and the melting process completed in a few seconds (Fig. 2I and movie S4). IR laser was also effective for melting the liquid metal droplets in a noncontact manner (Fig. 2J). The heat generated by the IR laser is constrained at the laser spot and thus can be leveraged to realize localized melting of the liquid metal inclusion (Fig. 2K). Both Joule heating and IR heating provide fast yet readily controllable melting mechanisms for reverting the solidification process. Afterward, the liquid metal inclusion returns to its supercooling state, and the samples can be reused. Compared to previous reports, the diversity of the demonstrated strategies in terms of both solidification and melting control of the phase change inclusion and the application potential of our material system are unpaired (table S2 and table S3).

We proceeded by showing that the multi-stimulus responsive LMEA can perceive different forms of information-encoded stimuli and translate them into thermal patterns. The compression stress induced by continuous handwriting was used to trigger the solidification of the liquid metal inclusion for real-time IR patterning. It is notable that the handwriting tracks, i.e., the letters "A" and "B," were visible to IR imaging but invisible to bare eyes (Fig. 3A and movie S5). Monitoring the time-dependent temperature in the region on the handwriting track showed an abrupt temperature increase upon writing. It took a relatively long period of about 100 s for its temperature to drop back to ambient temperature via natural heat dissipation, after which the IR patterns were erased (fig. S25). This mechanism was further used for detecting compressive impact by solid objects (Fig. 3B) and flow impinging by pressurized gases (fig. S26). When solid spheres were made to impact on the LMEA, localized solidification and temperature increase created circular IR regions (Fig. 3B). By analyzing the IR images, information regarding the impact location (in a Cartesian coordinate) and the size of the spheres was obtained (fig. S27).

A magnetic field was used to trigger the solidification of predefined patterns of the LMEA to demonstrate noncontact realization of programable IR patterning. This was first demonstrated with arrays of circular LMEA pixels embedded into an elastomer substrate (Fig. 3C). The solidification and heat release of each pixel could be triggered individually in any selected sequence, and one example was given in Fig. 3C (movie S6). IR display of more complex

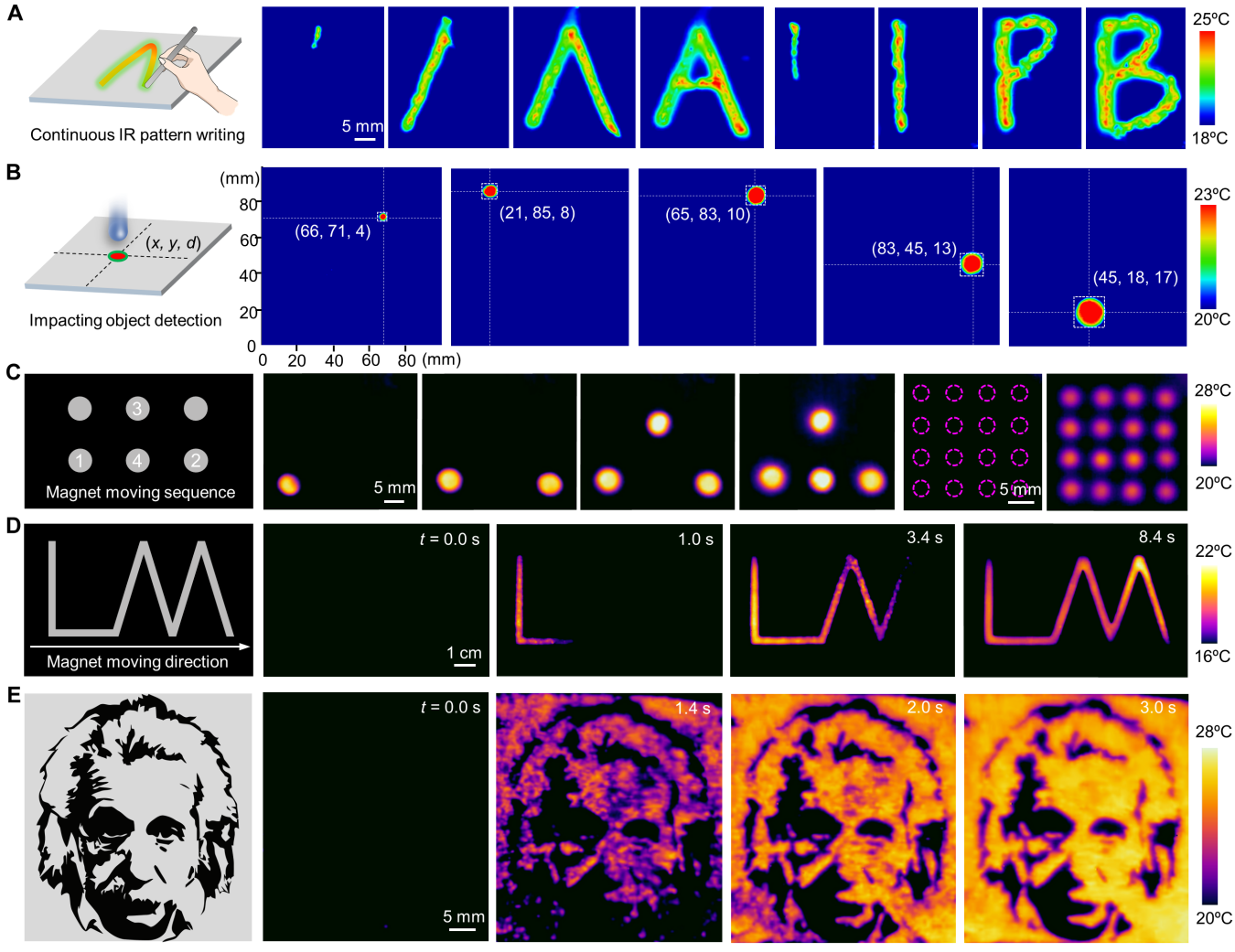

Fig. 3. Perception of information-encoded triggering signals and real-time IR visualization by the LMEA. (**A**) Schematic and IR imaging of continuous handwriting on the surface of LMEA. (**B**) Schematic and IR imaging of spherical objects of varied sizes affecting on a LMEA film. Both the impact location and the size of the spheres were indicated. (**C**) Pixelated IR display using magnetic field–triggered solidification of LMEA pixel arrays. (**D** and **E**) Continuous IR imaging of predefined complex patterns based on magnetic field–triggered solidification of LMEA. The regions colored gray in the schematics of (A) to (E) represent the LMEA regions.

patterns was achievable using pixel arrays made of the LMEA (Fig. 3C).

In addition, continuous IR display of complex patterns was also achieved. We fabricated a "LM"-shaped LMEA pattern (gray regions, Fig. 3D) and applied a magnetic field to the pattern from left to right. The IR image of the pattern appeared in a continuous way following the moving direction of the magnet, indicating the gradual solidification of its liquid metal inclusion (Fig. 3D and movie S7). The samples could be reused once the liquid metal inclusion was remelted and supercooled (fig. S28). To demonstrate the capability of the LMEA for generating complex thermal patterns, the material was fabricated to display a detailed portrait (gray regions in Fig. 3E). Delicate and sharp IR features defined by the liquid metal-elastomer and elastomer-only regions were observed (movie S8), indicating excellent resolutions at millimeter levels and above. This was attributed to the distinct thermal conductivity between the LMEA and the elastomer, and the less thermally conductive elastomer suppressed the heat diffusion toward it, leading to a large temperature gradient between the two and thus a high thermal imaging resolution (fig. S29).

The released thermal energy of the LMEA so far was visualizable through imaging in the IR wavelength region but not the visible region (Figs. 1 and 3). A thermochromic particulate inclusion was further added during the fabrication process to realize thermochromic visualization. Having a low density, the thermochromic particles were found to accumulate in the elastomer-rich layer (Fig. 4A), which showed negligible effect on the phase transition behaviors of the liquid metal inclusion. The resulting thermochromic LMEA (TC-LMEA) allowed visualization in both the visible and IR spectrum regions (the surface on the elastomer layer side was used for thermal and optical imaging for TC-LMEA samples). The TC-LMEA inherited the multistimulus responsiveness to contact mechanical (Fig. 4B and fig. S30) and noncontact magnetic stimuli (fig. S31). The temperature increase induced by the solidification of the liquid metal inclusion

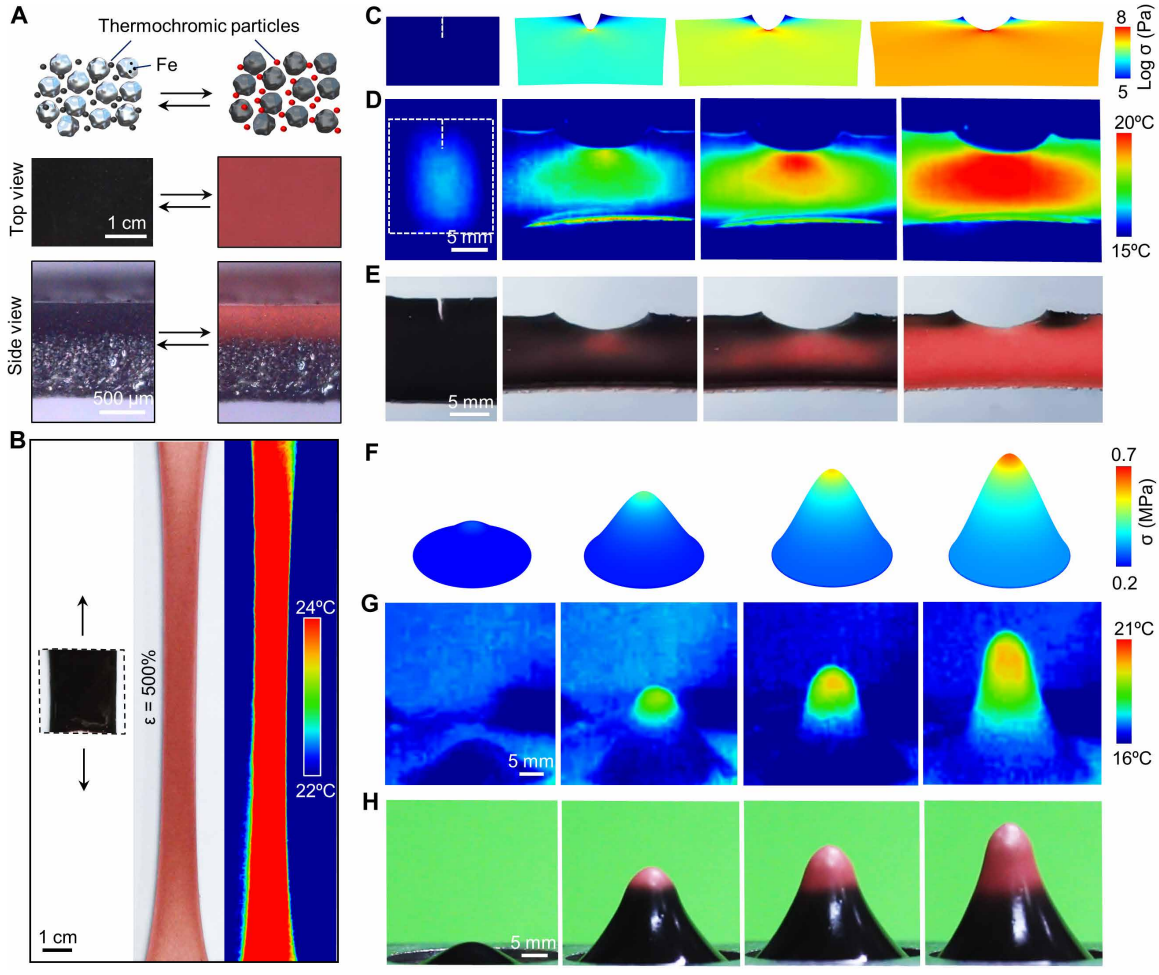

Fig. 4. TC-LMEA for IR and optical perception and visualization. (**A**) Schematic diagram (top), top-view (middle), and side view (bottom) of the elastomer with magnetized liquid metal droplets and thermochromic particles inclusions during phase transition. (**B**) Optical image and thermal image showing the color change and temperature increase of a TC-LMEA sample under stretching. (**C** to **E**) Snapshots of stress distribution by finite element analysis (C), thermal field by IR imaging (D), and optical color change (E) of a stretched TC-LMEA film with a cut on one edge. (**F** to **H**) Snapshots of stress distribution by finite element simulation (F), thermal field by IR imaging (G), and optical color change (H) of a circular TC-LMEA film poked at its center.

simultaneously generated a visible color change due to the presence of the thermochromic inclusion together with a matching IR pattern.

In what follows, we demonstrated the unprecedented capability of the TC-LMEA for perceiving and self-visualization dynamic stress evolution processes within the stretchable material. It is well known that, when an elastic rectangular strip with a crack (notch) on its edge is stretched biaxially, stress concentration occurs at the tip of the crack, which leads to further propagation of the crack. This was revealed in our finite element analysis of a stretched strip of the TC-LMEA (Fig. 4C and note S2) (*48*). In excellent agreement with theory and simulation, such a stress concentration at the crack tip of the stretched TC-LMEA was shown in both the IR temperature profile (Fig. 4D and movie S9) and the optical time lapse (Fig. 4E and movie S10). When the material was under biaxial stretching, the crack tip experienced the maximum tensile stress and first reached the threshold stress for triggering the solidification of the liquid metal inclusion. Consequently, temperature increase and the accompanying thermochromic color change were first observed at the crack tip. Under continuous stretching and crack propagation, the increasing stress and strain triggered the liquid metal inclusion in the surrounding area to continually solidify, and consequently, the high-temperature region spread outward from the crack site. A control experiment with a crack-free specimen was performed, which did not show such a stress concentration and the corresponding temperature gradient (fig. S32 and movie S11). The stress evolution and distribution visualization of a circular TC-LMEA film during out-of-plane deformation (poking) was further accessed (Fig. 4, F to H). As shown in the finite element analysis, when poked at its center, the maximum deformation and maximum stress of the thin elastic film occurred at the apical, which decreased radially toward its rim (Fig. 4F). Therefore, the stress at the apex was expected to first reach the threshold to trigger phase transition and latent heat release therein. Localized temperature increase (Fig. 4G) and color change (Fig. 4H and movie S12) at the apical region indeed validated such a stress distribution. As the poking proceeded, the high temperature region propagated downhill radially.

DISCUSSION

We demonstrated a highly stretchable LMEA, which was able to respond to various forms of contact and noncontact stimuli via controllable phase transition. The incorporation of magnetic Fe particles into the liquid metal inclusion was found to be crucial for realizing sensitive multi-stimulus–responsive solidification control. The design concept of the soft architecture was extended to different liquid metals as the inclusions and different soft materials as the host matrices. Treating the thermal energy flow as an information carrier, we used the LMEA as a soft platform for perceiving and visualizing different forms of information-coded stimuli and translated them into IR and visible color patterns. Moreover, the LMEA showed unprecedented self-recognition and self-display capabilities of highly dynamic stress distribution and evolution processes in fine details. Strategies for melting the solidified phase change inclusion were demonstrated to achieve two-way phase transition control. The solidification can lead to mechanical stiffening and plastic deformation, and the thermal diffusion can cause visualization delays, which can become limiting in certain applications and need to be addressed with improved material design. Given the demonstrated generic design principle, multi-stimulus response, tunable working temperature range, achievable sensitivity, and resolution, it is believed that the LMEA can enable a wide range of applications in intelligent display, stress visualization, information encryption, motion detection, as well as other multi-stimulus responsive systems with thermal-mechanical, thermal-magnetic, and/or thermal-chromic integration. In this regard, the present work provides a rational soft architecture design and a sensitive, controllable phase transition mechanism for achieving integrated functionalities and soft intelligence.

MATERIALS AND METHODS

Preparation of Fe-containing LMEA

We chose Ga (Nanjing Jinmei Gallium Ltd., 99.999%) as a main model of liquid metal to fabricate the LMEA owing to its favorable melting point (29.8°C). The preparation of LMEA began with the fabrication of magnetic liquid metal. In this step, melted Ga (or other liquid metals) and solid Fe particles (diameter, ~30 μm) were added into a beaker with the addition of 3 M hydrochloric acid (HCl) solution (*50*), which were stirred for 10 min until the Fe particles were dispersed in the liquid metal. The mixture was then washed with deionized water to remove the residual HCl solution and dried in a vacuum oven. Following the above steps, which may need repeated a few times to obtain the high loading of Fe particles, the magnetized (Fe-incorporated) liquid metal was prepared. The fabrication was conducted on a hot plate with a temperature of about 40°C to keep the Ga in liquid status during the whole process. The ratio of Fe particles in magnetic liquid metal was 20 wt % to realize a good balance of the good fluidity and magnetic responsiveness. Further, the LMEA was prepared by stirring the magnetized (Fe-incorporated) liquid metal together with the uncured silicone elastomer part A (Pt-catalyzed polymethylhydrosiloxane) and part B (methyl vinyl polysiloxane) at 1:1 volume ratio of the two. The liquid metal was fragmented into micrometer-level droplets, which were well dispersed in the viscous medium after stirring (*51*). The mixture was then cured at room temperature in different molds to obtain the LMEA samples, during which the size-dependent sedimentation of the liquid metal droplets took place.

Liquid metal inclusion-elastomer with a weight ratio of 3:2 led to overall the best performance of the LMEAs in terms of its magnetic response, phase transition heat release, and stretchability, among all the ratios tested in this study. Unless otherwise specified, these ratios remain constant throughout this work. The magnetized (Fe-incorporated) liquid metal was stirred for 2 min at the speed of 500 rpm to obtain desirable performance. Longer stirring time led to the smaller size of liquid metal droplets, making it less efficient to achieve the stimuli-responsive phase transition. Moreover, larger liquid metal droplet size (with a shorter stirring time) may lead to unpredictable leakage and reduced resolution of the thermal pattern. To show the universality of materials synthesis, PDMS and Ecoflex were also chosen as the matrix to suspend the magnetized (Fe-incorporated) liquid metal droplets. To investigate the influence of Fe particle internalization on magnetic-responsive solidification, the elastomer with Fe particles and Ga droplets was fabricated by directly mixing for 2 min at the speed of 500 rpm, where the Fe particles were outside of liquid metal droplets.

Fabrication of LMEA with different liquid metal inclusions (varied phase change temperature)

To regulate the working temperature of LMEA, liquid metals with different melting points were selected as the phase change inclusions in LMEA. The binary alloy (EGaIn) and ternary alloys (BiInSn and Galinstan) with low melting points were fabricated. EGaIn is composed of 75.5% Ga and 24.5% indium by weight (*52*), which is prepared by heating raw metals in a beaker on a hot plate (200°C) and mixing for 20 min. To fabricate the BiInSn alloy, bismuth, indium, and tin with weight ratios of 31.6, 48.8, and 19.6%, respectively, were added into a beaker and then heated (250°C) for 30 min until the metals completely mixed. Then, the mixture was stirred for 20 min to obtain uniform BiInSn alloy. Galinstan is composed of 68.5% Ga, 21.5% indium, and 10% tin by weight (*53*), which was prepared using the above methods. The fabrication of Fe-incorporated liquid metal with different melting points was similar to the Fe-incorporated Ga. With continuous stirring, the magnetized liquid metals with different melting points were obtained by introducing Fe particles into different liquid metals in the HCl solutions. The residual acid solution was removed by deionized water and then dried in a vacuum oven. The magnetized liquid metals were molten and then mixed thoroughly into the uncured elastomer. It is noteworthy that the fabrication temperature should be well controlled to ensure their molten state. After being cured, the LMEA with different liquid metal inclusions was prepared. It should be noted that the LMEA (BiInSn) fabrication differed from others due to the high operation temperature (~70°C). To avoid violent chemical reaction, Fe particles with a relatively larger size (100 μm) were selected to fabricate the magnetized liquid metal. In terms of mixing with uncured elastomer, the molten liquid metal was dispersed in elastomer part A (Pt-catalyzed polymethylhydrosiloxane) and then mixed with part B (methyl vinyl polysiloxane) to avoid immediate curing caused by heat in the process, which may lead to non-uniform mixing.

Fabrication of TC-LMEA

The thermochromic powders (Bichrom T Series, Insilico company, Korea) with an average diameter of 2 to 5 μm were mixed into uncured elastomer via stirring for 2 min (500 rpm) and then magnetized liquid metal was added to the elastomer to prepare the

TC-LMEA. Here, the color of thermochromic powders can switch between black (cooled) and red (heated) reversibly by temperature regulation. Therefore, the thermal energy generated from the prompt solidification of liquid metal inclusions can be translated into the color change of the LMEA sample from black to red, which enables the visualization of the information-encoded stimuli and developmental solidification. Thermochromic powders with a transition point at 18°C were occupied in most of the experiments, except for Fig. 4B where another thermochromic powder with a transition point at 22°C was applied. Because of the density difference, thermochromic powders tend to accumulate in the upper elastomer-rich layer, while the liquid metal inclusions were located at the bottom layer during curing. Therefore, there is a time delay in observing the color change of the upper layer and the solidification of liquid metal inclusions due to the heat transfer time from the bottom layer to the upper layer. We stretched the LMEA quickly and observed the color change process in a fixed strain. The spatial color change as a function of time at the fixed strain could be recognized as an alternative parameter to monitoring the stress evolution during stretching.

Characterizations of LMEA

To gain a complete understanding of the internal structure of LMEA, the three-dimensional structure of LMEA was obtained by micro-CT (Carl Zeiss Xradia 410 versa, Germany). The size distribution of liquid metal droplets was analyzed by the software ImageJ. IR images were collected and processed with a Fotric 220S IR camera and the AnalyzIR software, respectively. The rectangular samples of LMEA were stretched biaxially with a speed of about 6 cm s^{-1}. Magnetic field was generated by cyclically moving a permanent magnet (200 mT) (average frequency of 3 Hz). Magnetic field strength was measured by a magnetometer. The cross section of LMEA was obtained by cutting the frozen sample (solidified). Magnetic hysteresis loops of the LMEA and elastomer with Ga inclusion were tested using a vibrating sample magnetometer at 298 K. A metallographic microscope was applied to obtain LMEA micrographs. Scanning electron microscopy and EDS images of the cross section were acquired by a Hitachi SU-8010 electron microscope. The EDS spectroscopy and mapping analysis were conducted with an accelerating voltage of 15 kV. The phase change behaviors of the elastomer and LMEA were measured by a NETZSCH DSC system (NETZSCH DSC200F3, Germany). The storage modulus and loss modulus were tested by a Dynamic Thermomechanical Analysis Q800 instrument. Stress-strain tests were performed using a tensile testing machine with a speed of 5 mm/s (WDW3020). Stress-strain behaviors of the LMEA were taken under 15°C when the LM filler was either supercooled or solidified and under 35°C when the LM filler was melted, respectively. Airflow was generated by an air pump. Steel marbles with different diameters were shot by a slingshot at a distance of 50 cm.

The electrical properties of LMEA were tested by a multimeter. These experiments were done under 15°C, and the bottom side of a LMEA sample (dimension: 16 mm by 13 mm by 2 mm) was selected to measure the electrical conductivity. When a magnetic field (200 mT) was applied, the supercooled liquid metal inclusion solidified, and the resistance decreased markedly (~10^8 times). The LMEA was directly heated on a hot plate (50°C) to melt the liquid metal inclusion.

LMEA heating for melting liquid metal inclusion

Laser heating

In the near IR laser heating experiments, the materials were exposed to an 808-nm laser at the energy density of 1 W/cm^2. A red spot was observed during the laser irradiation, which resulted from the inclusion of visible wavelength in the laser bandwidth.

Joule heating

To generate Joule heat, two alligator clips were applied at both ends of the sample under the voltage of 5 V. The change of temperature and the microstructure of the bottom surface of the LMEA during the whole procedure were recorded by an IR camera and a microscope, respectively.

Other (direct) heating methods

Heating devices such as temperature-regulated chambers, plates, and hot air guns were used to accommodate different purposes.

Shape change induced by the phase transition of liquid metal inclusion in LMEA

To evaluate the deformation ability of supercooled LMEA, the tensile experiment was conducted at 10°C. The sample was stretched biaxially and then released from one side. In the demonstration of grasping, an object (pencil) was placed at the middle of the stretched sample (solidified). Upon releasing one side of the sample, the pencil was securely rolled up by the contracted and curled sample. By lifting the thin wire tied to the sample, the object was manipulated and then released by remelting the liquid metal inclusions through the laser irradiation.

Supplementary Materials

This PDF file includes:

Supplementary Notes S1 and S2
Fig. S1 to S32
Tables S1 to S3
Legends for movies S1 to S12
References

Other Supplementary Material for this manuscript includes the following:

Movies S1 to S12

REFERENCES AND NOTES

1. W. Hu, G. Z. Lum, M. Mastrangeli, M. Sitti, Small-scale soft-bodied robot with multimodal locomotion. *Nature* **554**, 81–85 (2018).
2. D. Rus, M. T. Tolley, Design, fabrication and control of soft robots. *Nature* **521**, 467–475 (2015).
3. S. Wang, J. Xu, W. Wang, G.-J. N. Wang, R. Rastak, F. Molina-Lopez, J. W. Chung, S. Niu, V. R. Feig, J. Lopez, T. Lei, S.-K. Kwon, Y. Kim, A. M. Foudeh, A. Ehrlich, A. Gasperini, Y. Yun, B. Murmann, J. B.-H. Tok, Z. Bao, Skin electronics from scalable fabrication of an intrinsically stretchable transistor array. *Nature* **555**, 83–88 (2018).
4. Z. Ma, Q. Huang, Q. Xu, Q. Zhuang, X. Zhao, Y. Yang, H. Qiu, Z. Yang, C. Wang, Y. Chai, Z. Zheng, Permeable superelastic liquid-metal fibre mat enables biocompatible and monolithic stretchable electronics. *Nat. Mater.* **20**, 859–868 (2021).
5. J. Li, Y. Liu, L. Yuan, B. Zhang, E. S. Bishop, K. Wang, J. Tang, Y. Q. Zheng, W. Xu, S. Niu, L. Beker, T. L. Li, G. Chen, M. Diyaolu, A. L. Thomas, V. Mottini, J. B. Tok, J. C. Y. Dunn, B. Cui, S. P. Pasca, Y. Cui, A. Habtezion, X. Chen, Z. Bao, A tissue-like neurotransmitter sensor for the brain and gut. *Nature* **606**, 94–101 (2022).
6. H. Na, Y. W. Kang, C. S. Park, S. Jung, H. Y. Kim, J. Y. Sun, Hydrogel-based strong and fast actuators by electroosmotic turgor pressure. *Science* **376**, 301–307 (2022).
7. Z. C. Liu, H. K. Bisoyi, Y. L. Huang, M. Wang, H. Yang, Q. Li, Thermo- and mechanochromic camouflage and self-healing in biomimetic soft actuators based on liquid crystal elastomers. *Angew. Chem. Int. Ed. Engl.* **61**, e202115755 (2022).
8. H. Q. Wang, Y. Q. Tang, Z. Y. Huang, F. Z. Wang, P. F. Qiu, X. F. Zhang, C. H. Li, Q. Li, A dual-responsive liquid crystal elastomer for multi-level encryption and transient information display. *Angew. Chem. Int. Ed. Engl.* **135**, e202313728 (2023).

9. B. F. Ding, P. Y. Zeng, Z. Y. Huang, L. X. Dai, T. S. Lan, H. Xu, Y. K. Pan, Y. T. Luo, Q. M. Yu, H. M. Cheng, B. L. Liu, A 2D material-based transparent hydrogel with engineerable interference colours. *Nat. Commun.* **13**, 1212 (2022).
10. Z. Y. Huang, T. S. Lan, L. X. Dai, X. T. Zhao, Z. Y. Wang, Z. H. Zhang, B. Li, J. L. Li, J. A. Liu, B. F. Ding, A. K. Geim, H. M. Cheng, B. L. Liu, 2D Functional Minerals as Sustainable Materials for Magneto-Optics. *Adv. Mater.* **34**, e2110464 (2022).
11. J. Li, A. D. Celiz, J. Yang, Q. Yang, I. Wamala, W. Whyte, B. R. Seo, N. V. Vasilyev, J. J. Vlassak, Z. Suo, D. J. Mooney, Tough adhesives for diverse wet surfaces. *Science* **357**, 378–381 (2017).
12. N. Li, Y. Li, Z. Cheng, Y. Liu, Y. Dai, S. Kang, S. Li, N. Shan, S. Wai, A. Ziaja, Y. Wang, J. Strzalka, W. Liu, C. Zhang, X. Gu, J. A. Hubbell, B. Tian, S. Wang, Bioadhesive polymer semiconductors and transistors for intimate biointerfaces. *Science* **381**, 686–693 (2023).
13. T. Matsuda, R. Kawakami, R. Namba, T. Nakajima, J. P. Gong, Mechanoresponsive self-growing hydrogels inspired by muscle training. *Science* **363**, 504–508 (2019).
14. Z. Pei, Y. Yang, Q. Chen, E. M. Terentjev, Y. Wei, Y. Ji, Mouldable liquid-crystalline elastomer actuators with exchangeable covalent bonds. *Nat. Mater.* **13**, 36–41 (2014).
15. C. Kaspar, B. Ravoo, W. G. van der Wiel, S. Wegner, W. Pernice, The rise of intelligent matter. *Nature* **594**, 345–355 (2021).
16. A. Chortos, J. Liu, Z. Bao, Pursuing prosthetic electronic skin. *Nat. Mater.* **15**, 937–950 (2016).
17. J. Gao, Y. Tang, D. Martella, J. Guo, D. S. Wiersma, Q. Li, Stimuli-responsive photonic actuators for integrated biomimetic and intelligent systems. *Respons. Mater.* **1**, e20230008 (2023).
18. Y. N. Xu, B. F. Ding, Z. Y. Huang, L. X. Dai, P. Liu, B. Li, W. Cai, H. M. Cheng, B. L. Liu, Deep ultraviolet hydrogel based on 2D cobalt-doped titanate. *Light-Sci. Appl.* **12**, 1 (2023).
19. H. K. Bisoyi, Q. Li, Liquid crystals: Versatile self-organized smart soft materials. *Chem. Rev.* **122**, 4887–4926 (2021).
20. Y. Kim, H. Yuk, R. Zhao, S. A. Chester, X. Zhao, Printing ferromagnetic domains for untethered fast-transforming soft materials. *Nature* **558**, 274–279 (2018).
21. C. Liu, H. Huang, Y. Wu, S. Fan, Thermal conductivity improvement of silicone elastomer with carbon nanotube loading. *Appl. Phys. Lett.* **84**, 4248–4250 (2004).
22. Y. Song, N. Wang, C. Hu, Z. L. Wang, Y. Yang, Soft triboelectric nanogenerators for mechanical energy scavenging and self-powered sensors. *Nano Energy* **84**, 105919 (2021).
23. M. Sitti, Physical intelligence as a new paradigm. *Extreme Mech. Lett.* **46**, 101340 (2021).
24. S. Mei, Y. Gao, Z. Deng, J. Liu, Thermally conductive and highly electrically resistive grease through homogeneously dispersing liquid metal droplets inside methyl silicone oil. *J. Electron. Packag.* **136**, 011009 (2014).
25. G. L. Yun, T. Cole, Y. X. Zhang, J. H. Zheng, S. S. Sun, Y. Ou-yang, J. Shu, H. D. Lu, Q. T. Zhang, Y. J. Wang, D. Pham, T. Hasan, W. H. Li, S. W. Zhang, S. Y. Tang, Electro-mechano responsive elastomers with self-tunable conductivity and stiffness. *Sci. Adv.* **9**, eadf1141 (2023).
26. Q. C. Shen, M. D. Jiang, R. T. Wang, K. X. Song, M. H. Vong, W. J. Jung, F. Krisnadi, R. Y. Kan, F. Y. Zheng, B. W. Fu, P. Tao, C. Y. Song, G. M. Weng, B. Peng, J. Wang, W. Shang, M. D. Dickey, T. Deng, Liquid metal-based soft, hermetic, and wireless-communicable seals for stretchable systems. *Science* **379**, 488–493 (2023).
27. A. Fassler, C. Majidi, Liquid-phase metal inclusions for a conductive polymer composite. *Adv. Mater.* **27**, 1928–1932 (2015).
28. Y. Peng, Y. Xin, J. Zhang, M. D. Dickey, Q. Li, Functional heterophasic liquid metals. *Respons. Mater.* **1**, e20230003 (2023).
29. W. Lee, H. Kim, I. Kang, H. Park, J. Jung, H. Lee, H. Park, J. S. Park, J. M. Yuk, S. Ryu, Universal assembly of liquid metal particles in polymers enables elastic printed circuit board. *Science* **378**, 637–641 (2022).
30. M. D. Bartlett, N. Kazem, M. J. Powell-Palm, X. Huang, W. Sun, J. A. Malen, C. Majidi, High thermal conductivity in soft elastomers with elongated liquid metal inclusions. *Proc. Natl. Acad. Sci. U.S.A.* **114**, 2143–2148 (2017).
31. H. Wang, Y. Yao, Z. He, W. Rao, L. Hu, S. Chen, J. Lin, J. Gao, P. Zhang, X. Sun, A highly stretchable liquid metal polymer as reversible transitional insulator and conductor. *Adv. Mater.* **31**, e1901337 (2019).
32. H. Liu, Y. Xin, H. K. Bisoyi, Y. Peng, J. Zhang, Q. Li, Stimuli-driven insulator–conductor transition in a flexible polymer composite Enabled by biphasic liquid metal. *Adv. Mater.* **33**, e2104634 (2021).
33. G. Yun, S.-Y. Tang, S. Sun, D. Yuan, Q. Zhao, L. Deng, S. Yan, H. Du, M. D. Dickey, W. Li, Liquid metal-filled magnetorheological elastomer with positive piezoconductivity. *Nat. Commun.* **10**, 1300 (2019).
34. E. J. Markvicka, M. D. Bartlett, X. Huang, C. Majidi, An autonomously electrically self-healing liquid metal–elastomer composite for robust soft-matter robotics and electronics. *Nat. Mater.* **17**, 618–624 (2018).
35. C. Pan, E. J. Markvicka, M. H. Malakooti, J. Yan, L. Hu, K. Matyjaszewski, C. Majidi, A liquid-metal–elastomer nanocomposite for stretchable dielectric materials. *Adv. Mater.* **31**, e1900663 (2019).
36. H. Wang, W. Xing, S. Chen, C. Song, M. D. Dickey, T. Deng, Liquid metal composites with enhanced thermal conductivity and stability using molecular thermal linker. *Adv. Mater.* **33**, e2103104 (2021).
37. M. Q. Zeng, L. Y. Li, X. H. Zhu, L. Fu, A liquid metal reaction system for advanced material manufacturing. *Acc. Chem. Res.* **2**, 669–680 (2021).
38. B. S. Chang, R. Tutika, J. Cutinho, S. Oyola-Reynoso, J. Chen, M. D. Bartlett, M. M. Thuo, Mechanically triggered composite stiffness tuning through thermodynamic relaxation (ST3R). *Mater. Horiz.* **5**, 416–422 (2018).
39. S.-H. Byun, J. Y. Sim, Z. Zhou, J. Lee, R. Qazi, M. C. Walicki, K. E. Parker, M. P. Haney, S. H. Choi, A. Shon, Mechanically transformative electronics, sensors, and implantable devices. *Sci. Adv.* **5**, eaay0418 (2019).
40. L. J. Elston, J. Ervin, Thermal history characterization and controlled nucleation of supercooled gallium. *J. Thermophys. Heat. Tr.* **34**, 358–370 (2020).
41. A. Di Cicco, Phase transitions in confined gallium droplets. *Phys. Rev. Lett.* **81**, 2942–2945 (1998).
42. J. Tang, S. Lambie, N. Meftahi, A. J. Christofferson, J. Yang, M. B. Ghasemian, J. Han, F. M. Allioux, M. A. Rahim, M. Mayyas, T. Daeneke, C. F. McConville, K. G. Steenbergen, R. B. Kaner, S. P. Russo, N. Gaston, K. Kalantar-Zadeh, Unique surface patterns emerging during solidification of liquid metal alloys. *Nat. Nanotechnol.* **16**, 431–439 (2021).
43. M. H. Malakooti, N. Kazem, J. Yan, C. Pan, E. J. Markvicka, K. Matyjaszewski, C. Majidi, Liquid metal supercooling for low-temperature thermoelectric wearables. *Adv. Funct. Mater.* **29**, 1906098 (2019).
44. A. Martin, B. S. Chang, A. M. Pauls, C. Du, M. Thuo, Stabilization of undercooled metals via passivating oxide layers. *Angew. Chem. Int. Ed. Engl.* **133**, 5993–6000 (2021).
45. B. Wang, J. Maslik, O. Hellman, A. Gumiero, K. Hjort, Supercooled liquid Ga stretchable electronics. *Adv. Funct. Mater.* **33**, 2300036 (2023).
46. J. Tang, X. Zhao, J. Li, Y. Zhou, J. Liu, Liquid metal phagocytosis: Intermetallic wetting induced particle internalization. *Adv. Sci.* **4**, 1700024 (2017).
47. S. W. Young, Mechanical stimulus to crystallization in supercooled liquids[1]. *J. Am. Chem. Soc.* **33**, 148–162 (1911).
48. See the Supplementary Materials.
49. M. H. Huang, C. Boone, M. Roberts, D. E. Savage, M. G. Lagally, N. Shaji, H. Qin, R. Blick, J. A. Nairn, F. Liu, Nanomechanical architecture of strained bilayer thin films: From design principles to experimental fabrication. *Adv. Mater.* **17**, 2860–2864 (2005).
50. H. Wang, B. Yuan, S. Liang, R. Guo, W. Rao, X. Wang, H. Chang, Y. Ding, J. Liu, L. Wang, PLUS-M: A porous liquid-metal enabled ubiquitous soft Material. *Mater. Horiz.* **5**, 222–229 (2018).
51. N. Kazem, T. Hellebrekers, C. Majidi, Soft multifunctional composites and emulsions with liquid metals. *Adv. Mater.* **29**, 1605985 (2017).
52. T. Daeneke, K. Khoshmanesh, N. Mahmood, I. A. De Castro, D. Esrafilzadeh, S. Barrow, M. Dickey, K. Kalantar-Zadeh, Liquid metals: Fundamentals and applications in chemistry. *Chem. Soc. Rev.* **47**, 4073–4111 (2018).
53. J. Zhang, L. Sheng, J. Liu, Synthetically chemical-electrical mechanism for controlling large scale reversible deformation of liquid metal objects. *Sci. Rep.* **4**, 7116 (2014).
54. O. C. Zienkiewicz, R. L. Taylor, *The finite element method for solid and structural mechanics*. (Elsevier, 2005).
55. I. M. Van Meerbeek, B. C. Mac Murray, J. W. Kim, S. S. Robinson, P. X. Zou, M. N. Silberstein, R. F. Shepherd, Morphing metal and elastomer bicontinuous foams for reversible stiffness, shape memory, and self-healing soft machines. *Adv. Mater.* **28**, 2801–2806 (2016).
56. C. B. Cooper, I. D. Joshipura, D. P. Parekh, J. Norkett, R. Mailen, V. M. Miller, J. Genzer, M. D. Dickey, Toughening stretchable fibers via serial fracturing of a metallic core. *Sci. Adv.* **5**, eaat4600 (2019).
57. G. Q. Li, M. Y. Zhang, S. H. Liu, M. Yuan, J. J. Wu, M. Yu, L. J. Teng, Z. W. Xu, J. H. Guo, G. L. Li, Z. Y. Liu, X. Ma, Three-dimensional flexible electronics using solidified liquid metal with regulated plasticity. *Nat. Electron.* **6**, 154–163 (2023).
58. L. F. Zhu, Y. Z. Chen, W. H. Shang, S. Handschuh-Wang, X. H. Zhou, T. S. Gan, Q. X. Wu, Y. Z. Liu, X. C. Zhou, Anisotropic liquid metal-elastomer composites. *J. Mater. Chem. C.* **7**, 10166–10172 (2019).
59. H. Liu, H. Tian, X. Li, X. Chen, K. Zhang, H. Shi, C. Wang, J. Shao, Shape-programmable, deformation-locking, and self-sensing artificial muscle based on liquid crystal elastomer and low–melting point alloy. *Sci. Adv.* **8**, eabn5722 (2022).
60. D. Hwang, E. J. Barron, A. B. M. T. Haque, M. D. Bartlett, Shape morphing mechanical metamaterials through reversible plasticity. *Sci. Robot.* **7**, eabg2171 (2022).
61. X. C. Ni, H. W. Luan, J. T. Kim, S. I. Rogge, Y. Bai, J. W. Kwak, S. L. Liu, D. S. Yang, S. Li, S. P. Li, Z. W. Li, Y. M. Zhang, C. S. Wu, X. Y. Ni, Y. G. Huang, H. L. Wang, J. A. Rogers, Soft shape-programmable surfaces by fast electromagnetic actuation of liquid metal networks. *Nat. Commun.* **13**, 5576 (2022).
62. Y. M. Xin, T. L. Gao, J. Xu, J. Y. Zhang, D. F. Wu, Transient electrically driven stiffness-changing materials from liquid metal polymer composites. *ACS Appl. Mater. Interfaces* **13**, 50392–50400 (2021).

63. S. Çinar, I. D. Tevis, J. H. Chen, M. Thuo, Mechanical fracturing of core-shell undercooled metal particles for heat-free soldering. *Sci. Rep.* **6**, 21864 (2016).
64. A. Martin, B. S. Chang, Z. Martin, D. Paramanik, C. Frankiewicz, S. Kundu, I. D. Tevis, M. Thuo, Heat-free fabrication of metallic interconnects for flexible/wearable devices. *Adv. Funct. Mater.* **29**, 1903687 (2019).
65. J. J. Chang, A. Martin, C. S. Du, A. M. Pauls, M. Thuo, Heat-free biomimetic metal molding on soft substrates. *Angew. Chem. Int. Ed. Engl.* **59**, 16346–16351 (2020).
66. H. Wang, Y. Peng, H. Peng, J. Y. Zhang, Fluidic phase-change materials with continuous latent heat from theoretically tunable ternary metals for efficient thermal management. *Proc. Natl. Acad. Sci. U.S.A.* **119**, e2200223119 (2022).
67. M. Yunusa, A. Lahlou, M. Sitti, Thermal effects on the crystallization kinetics, and interfacial adhesion of single-crystal phase-change gallium. *Adv. Mater.* **32**, e1907453 (2020).
68. C. L. Zhang, L. Li, Z. B. Li, H. Chang, J. Liu, Investigation on the spreading and solidification of supercooled gallium droplets during impact. *Int. J. Heat Mass Transf.* **183**, 122142 (2022).
69. Z. Ye, G. Z. Lum, S. Song, S. Rich, M. Sitti, Phase change of gallium enables highly reversible and switchable adhesion. *Adv. Mater.* **28**, 5088–5092 (2016).
70. H. S. Ge, J. Liu, Keeping smartphones cool with gallium phase change material. *J. Heat. Trans-T. Asme* **135**, 054503 (2013).
71. H. Wang, S. Chen, H. Li, X. Chen, J. Cheng, Y. Shao, C. Zhang, J. Zhang, L. Fan, H. Chang, R. Guo, X. Wang, N. Li, L. Hu, Y. Wei, J. Liu, A liquid gripper based on phase transitional metallic ferrofluid. *Adv. Funct. Mater.* **31**, 2100274 (2021).
72. X. Sun, B. Cui, B. Yuan, X. Wang, L. Fan, D. Yu, Z. He, L. Sheng, J. Liu, J. Lu, Liquid metal microparticles phase change medicated mechanical destruction for enhanced tumor cryoablation and dual-mode imaging. *Adv. Funct. Mater.* **30**, 2003359 (2020).
73. Y. Peng, H. Z. Liu, H. Peng, J. Y. Zhang, Biological self-healing strategies from mechanically robust heterophasic liquid metals. *Matter* **6**, 226–238 (2023).

Acknowledgments: We thank Q. Zheng, N. Li, X. Li, J. Zhang, M. Guo, and R. Li from Tsinghua University for assistance in collecting part of the experimental data. **Funding:** This work was partially supported by the National Natural Science Foundation of China under project 52301193, Key Project 91748206, and the China Postdoctoral Science Foundation under General Program 2021M691707. J.T. acknowledges the support from the Australian Research Council Discovery Early Career Researcher Award (DE220100816). **Author contributions:** Conceptualization: H.W., B.Y., J.T., and J.L.; investigation: H.W., X.Z., X.S., S.C., Y.C., X.Z., Y.Y., and B.W.; visualization: H.W., B.Y., W.D., K.D., R.G., and J.T.; funding acquisition: H.W., J.T., and J.L.; supervision: H.W., J.T., and J.L.; writing—original draft: H.W., B.Y., and J.T.; writing—review and editing: H.W., S.C., J.T., and J.L. **Competing interests:** The authors declare that they have no competing interests. **Data and materials availability:** All data needed to evaluate the conclusions in the paper are present in the paper and/or the Supplementary Materials.

Submitted 28 March 2024
Accepted 22 April 2024
Published 24 May 2024
10.1126/sciadv.adp5215